Angular distributions of photoelectrons from free Na clusters

P. Wopperer,[1] B. Faber,[2] P. M. Dinh,[1] P.-G. Reinhard,[2] and E. Suraud[1,2]

[1] *Université de Toulouse, UPS, Laboratoire de Physique Théorique, IRSAMC, F-31062 Toulouse Cedex, France and CNRS, UMR 5152, F-31062 Toulouse Cedex, France*

[2] *Institut für Theoretische Physik, Universität Erlangen, D-91058 Erlangen, Germany*

(Received 21 April 2010; revised manuscript received 1 December 2010; published 27 December 2010)

We explore, from a theoretical perspective, photoelectron angular distributions (PADs) of the Na clusters Na_8, Na_{10}, Na_{12}, Na_{18}, Na_3^+, Na_{11}^+, Na_{13}^+, and Na_{19}^+. The basis of the description is the time-dependent local-density approximation (TDLDA), augmented by a self-interaction correction (SIC) to describe ionization properties correctly. The scheme is solved on a numerical grid in coordinate space with absorbing bounds. We assume for each cluster system an isotropic ensemble of free clusters and develop for the case of one-photon emission analytical formulas for computing the orientation-averaged PAD on the basis of a few TDLDA-SIC calculations for properly chosen reference orientations. It turns out that all the information in the averaged PAD is contained in one anisotropy parameter. We find that this parameter varies very little with system size, but as a whole is crucially influenced by the detailed ionic structure. We also make comparisons with direct orientation averaging and consider one example reaching outside the perturbative regime.

DOI: 10.1103/PhysRevA.82.063416 PACS number(s): 33.80.Eh, 36.40.Mr, 36.40.Vz, 36.40.Wa

Photo-induced reactions have been used for decades as key tools to explore the properties of clusters. Optical absorption measurements give access both to structure and to dynamics of clusters; for an overview see [1–4]. Still, optical response can be valuably complemented by additional observables. A most important reaction channel is electron emission directly following an excitation by electromagnetic fields. There have thus been numerous investigations analyzing electrons emitted after irradiation by a short laser pulse. Beyond the mere net ionization yield, photoelectron spectroscopy (PES) measuring the distribution of the kinetic energy of emitted electrons is a tool of choice as it provides an energy-resolved cross section of electron emission; for early applications see [5,6]. The next (more involved) step is to analyze the photoelectron angular distribution (PAD). It supplies an angular-resolved description of the emission process. Such measurements have come up more recently and have usually combined PAD with PES, providing double differential cross sections (energy- and angular-resolved). First measurements dealt with the cluster anions: W_N^-, $N = 4$–11 [7,8]; Hg_N^-, $N = 3$–20 [9]; and C_N^-, $N = 10$–22 [10–12]. More recent results have been published for the C_{60} cluster [13] and medium-sized Na_N^- clusters [14,15]. The latter results nicely show a dependence of the photoemission on the electronic ground-state wave functions.

The theoretical description of photoelectron distributions has a long history in atomic physics [16]. It is usually treated in (multiphoton) perturbation theory [17]. See, for example, details for PAD from atoms in [18–20] and more recently an application of compact atomic expressions to spherical jellium metal clusters [21]. PADs have also been investigated theoretically in some molecular systems [22–24]. These methods require a good knowledge of the continuum states for the outgoing electrons and become more involved for clusters without any symmetry. On the other hand, many investigations, among the most robust and flexible ones, rely on time-dependent density-functional theory at the level of the local-density approximation (TDLDA) propagated directly in the time domain; see, e.g., [25–27]. This approach gives a convenient framework for analyzing electronic emission properties when augmented by a self-interaction correction (SIC) [28]. By introducing absorbing boundary conditions [29,30] and installing a careful bookkeeping of the directions of the absorbed (=emitted) electrons, one can develop a direct TDLDA-SIC description of photoangular distributions. It can be done quantum mechanically [31,32] for low excitations as well as in semiclassical approximation for more violent processes [33]. Angular distributions from free Na clusters with fixed orientation have been studied extensively in [31,32] and from Na clusters deposited on MgO(001) or Ar(001) substrates in [34]. A fixed cluster orientation is indeed naturally established when depositing the cluster on a substrate. But free clusters usually come along as an ensemble of clusters with *a priori* any orientation. The aim of this paper is to study PAD for rotationally invariant ensembles of free Na clusters within including a proper orientation averaging. The basis of the description remains the TDLDA-SIC of [31,32,34], but now augmented by averaging over an isotropic ensemble of orientations. We develop an exact averaging procedure for one-photon processes which only requires a limited number of actual TDLDA-SIC computations (actually six). The scheme is used to investigate PAD in some small Na_N and Na_N^+ clusters. We also explore more naive direct averaging schemes. The direct attack requires, of course, more reference orientations for proper sampling, but allows immediate application to any nonperturbative processes, for which we discuss one example.

The paper is outlined as follows: The formal framework is presented in Sec. I, developing in particular the analytical expressions for orientation averaging. The various results are presented and discussed in Sec. II.

I. FORMAL FRAMEWORK

A. Angular distributions from one-photon emission

The cross section for one-photon emission from the single-electron state ϕ_i is given in first-order perturbation theory

as [17]

$$\frac{d\sigma_i}{d\Omega} = \frac{4\pi^2 e^2 \omega_{\rm las}}{\hbar c} |\langle \psi_{k\vartheta\varphi} | \mathbf{e}_{\rm pol} \cdot \hat{\mathbf{r}} | \phi_i \rangle|^2 \equiv A^{(i)}(\vartheta\varphi), \quad (1)$$

where $\mathbf{e}_{\rm pol}$ is the direction of laser polarization, $|\phi_i\rangle$ the initial single-electron state from which the electron is removed, and $\psi_{k\vartheta\varphi}$ an outgoing wave which asymptotically becomes a plane wave traveling in direction $(\vartheta\varphi)$ with wave number k. The wave number is determined by the scattering conditions. It becomes $k = \sqrt{2m\varepsilon_{\rm out}}$, where $\varepsilon_{\rm out} = \varepsilon_i + \hbar\omega_{\rm las}$ with ε_i being the single-electron energy of the initial state and $\omega_{\rm las}$ the photon frequency. The symbol A is used here and in the following as an abbreviation for the cross section with indices indicating the particular context.

The cross section (1) applies to one fixed configuration in which the cluster orientation relative to laser polarization is known. In practice, one encounters an ensemble of clusters with arbitrary orientations. We have to evaluate the cross section for an ensemble of cluster orientations. To that end, we assume a situation without any bias on a certain direction, i.e., an isotropic ensemble in which all orientations appear with the same probability. For the evaluation, we distinguish the laboratory frame and the cluster frame (in which all quantities are primed). The laboratory frame is defined by the laser polarization such that the polarization vector points along the z axis, i.e., $\mathbf{e}_{\rm pol} = \mathbf{e}_z$. The observed emission angles $(\vartheta\varphi)$ are defined with respect to this laboratory frame, where ϑ is the angle against the z axis and φ the angle in the x-y plane. A cluster has three principle axes. The cluster orientation is defined as that of these three axes with respect to the laboratory frame. We start from a cluster in the laboratory frame where the major principle axis (a symmetry axis if available) is aligned with laser polarization. The rotated state i in the laboratory frame is obtained by

$$|\phi_{\alpha\beta\gamma,i}\rangle = \hat{D}(\alpha\beta\gamma)|\phi_i\rangle, \quad (2)$$

$$\hat{D}(\alpha\beta\gamma) = e^{i\alpha\hat{J}_z} e^{i\beta\hat{J}_y} e^{i\gamma\hat{J}_z}, \quad (3)$$

where $(\alpha\beta\gamma)$ are the three Euler angles [35]. The orientation-averaged one-photon excitation cross section for emission from the single-electron state ϕ_i then becomes

$$\overline{A^{(i)}}(\vartheta\varphi) = \int \frac{d\alpha d(\cos\beta) d\gamma}{8\pi^2} A^{(i)}(\vartheta\varphi,\alpha\beta\gamma), \quad (4)$$

with

$$A^{(i)}(\vartheta\varphi,\alpha\beta\gamma) = \frac{4\pi^2 e^2 \omega_{\rm las}}{\hbar c} |\langle \psi_{k\vartheta\varphi} | \mathbf{e}_{\rm pol} \cdot \hat{\mathbf{r}} | \phi_{\alpha\beta\gamma,i} \rangle|^2. \quad (5)$$

A conceptually simple way to compute this averaged cross section $\overline{A^{(i)}}$ is to define a finite element approximation to the integral over Euler angles, to compute the elementary cross section for the various orientations, and to sum over all results. This may become cumbersome if a fine mesh of Euler angles is used.

It is much more efficient, though more involved, to evaluate the angular integration analytically employing the well-known properties of the rotation matrices [35]. We introduce the following notations,

$$d^3\omega = \frac{d\alpha d(\cos\beta) d\gamma}{8\pi^2}, \quad \mathcal{N} = \frac{4\pi^2 e^2 \omega_{\rm las}}{\hbar c}, \quad (6)$$

and work out the given expressions in the cluster frame:

$$\begin{aligned} A'^{(i)}(\vartheta'\varphi',\alpha\beta\gamma) &= \mathcal{N} |\langle \psi'_{k\vartheta'\varphi'} | \mathbf{e}_{\rm pol} \cdot \hat{\mathbf{r}} | \phi'_{\alpha\beta\gamma,i} \rangle|^2 \\ &= \mathcal{N} |\langle \psi_{k\vartheta'\varphi'} | \mathbf{e}_{\rm pol} \cdot \hat{\mathbf{r}}' | \phi'_i \rangle|^2 \\ &= \sum_{\mu\mu'} D^{(1)*}_{0\mu}(\alpha\beta\gamma) D^{(1)}_{0\mu'}(\alpha\beta\gamma) A'^{(i)}_{\mu\mu'}(\vartheta'\varphi'), \end{aligned}$$

where

$$A'^{(i)}_{\mu\mu'}(\vartheta'\varphi') = \mathcal{N} \langle \psi_{k\vartheta'\varphi'} | \hat{r}'_\mu | \phi'_i \rangle \langle \phi'_i | (\hat{r}'_{\mu'})^* | \psi_{k\vartheta'\varphi'} \rangle$$

is the basic cross-section matrix in the cluster frame. The $D^{(1)}_{\nu\mu}$ are the well-known rotation matrices [35], $\hat{r}_\nu$ is the position operator in spherical representation, and $\hat{r}'_\mu$ is the analog in the cluster frame. For the next step, we exploit the fact that any reasonable function of $(\vartheta'\varphi')$ can be expanded in terms of spherical harmonics:

$$\begin{aligned} A'^{(i)}_{\mu\mu'}(\vartheta'\varphi') &= \sum_{lm'} a^{(i)}_{\mu\mu',lm'} Y_{lm'}(\vartheta'\varphi'), \\ a^{(i)}_{\mu\mu',lm'} &= \int d(\cos\vartheta') d\varphi' Y^*_{lm'} A'^{(i)}_{\mu\mu'}(\vartheta'\varphi'). \end{aligned} \quad (7)$$

The expression through Y_{lm} allows one to perform the rotation in the laboratory frame explicitly, yielding

$$A^{(i)}_{\mu\mu'}(\vartheta\varphi) = \sum_{lm'} a^{(i)}_{\mu\mu',lm'} \sum_m D^{(l)}_{mm'}(\alpha\beta\gamma) Y_{lm}(\vartheta\varphi)$$

and

$$\begin{aligned} A^{(i)}(\vartheta\varphi,\alpha\beta\gamma) = \sum_{\mu\mu',lmm'} & D^{(1)*}_{0\mu}(\alpha\beta\gamma) D^{(1)}_{0\mu'}(\alpha\beta\gamma) D^{(l)}_{mm'}(\alpha\beta\gamma) \\ & \times a^{(i)}_{\mu\mu',lm'} Y_{lm}(\vartheta\varphi). \end{aligned}$$

We insert these results into expression (4) for the averaged cross section, reorder integration and summations, and finally obtain

$$\begin{aligned} \frac{\overline{d\sigma_i}}{d\Omega} &= \sum_{\mu\mu'} \sum_{lm'} a^{(i)}_{\mu\mu',lm'} \sum_m Y_{lm}(\vartheta\varphi) \int d^3\omega\, D^{(1)*}_{0\mu}(\alpha\beta\gamma) \\ &\quad \times D^{(1)}_{0\mu'}(\alpha\beta\gamma) D^{(l)}_{mm'}(\alpha\beta\gamma) \\ &= \sum_{\mu\mu'} \sum_{lm'} a^{(i)}_{\mu\mu',lm'} \sum_m Y_{lm}(\vartheta\varphi) (-1)^\mu \begin{pmatrix} 1 & 1 & l \\ 0 & 0 & m \end{pmatrix} \\ &\quad \times \begin{pmatrix} 1 & 1 & l \\ -\mu & \mu' & m' \end{pmatrix}, \end{aligned}$$

where the large round brackets denote the Wigner $3j$ symbols [35]. The selection rules embodied in the $3j$ symbols shrink the summation to a simple final form for the averaged cross section:

$$\frac{\overline{d\sigma_i}}{d\Omega} = C^{(i)}_0 Y_{00}(\vartheta\varphi) + C^{(i)}_2 Y_{20}(\vartheta\varphi), \quad (8)$$

$$C^{(i)}_0 = \frac{1}{3} \sum_\mu a^{(i)}_{\mu\mu,00}, \quad (9)$$

$$C^{(i)}_2 = \sum_\mu a^{(i)}_{\mu\mu',2\,\mu-\mu'} (-1)^\mu \begin{pmatrix} 1 & 1 & 2 \\ 0 & 0 & 0 \end{pmatrix} \begin{pmatrix} 1 & 1 & 2 \\ -\mu & \mu' & \mu-\mu' \end{pmatrix}, \quad (10)$$

where the coefficients $a^{(i)}_{\mu\mu',lm'}$ are computed from angular momentum projection (7) of the cross sections $A'^{(i)}_{\mu\mu'}$ in the cluster frame.

It is important to note that the final coefficients C_{l0} only require the information about a very limited number of coefficients $a^{(i)}_{\mu\mu',lm'}$. We have $l = 0$ or 2 and $m' = \mu - \mu'$. This leaves three coefficients $a^{(i)}_{\mu\mu,00}$ for $l = 0$ and six coefficients $a^{(i)}_{\mu\mu',2\,\mu-\mu'}$ for $l = 2$ (note that the exchange $\mu \leftrightarrow \mu'$ does not need new information). Equation (7) shows that the different l can be produced from one distribution. We thus only need six different angular distributions in properly chosen (i.e., sufficiently different) polarization directions $\mathbf{e}^{(n)}_{\rm pol}$, $n = 1, \ldots, 6$: we compute the corresponding cross sections in the cluster frame $\sum_{\mu\mu'} e^{(n)}_{{\rm pol},\mu} A'^{(i)}_{\mu\mu'}(\vartheta'\varphi') e^{(n)}_{{\rm pol},\mu'}$ and project into the mix of coefficients $\sum_{\mu\mu'} e^{(n)}_{{\rm pol},\mu} a^{(i)}_{\mu\mu',l\mu-\mu'} e^{(n)}_{{\rm pol},\mu'}$ for $l = 0$ and 2 as well as for $n = 1, \ldots, 6$. Thus we have six linearly independent pieces of information from which we can compute the wanted coefficients $a^{(i)}_{\mu\mu',l\mu-\mu'}$ by solving a simple linear equation. The result is inserted into Eqs. (9) and (10) which finally yields the averaged cross section. This procedure involves a calculation of the cross sections in the cluster frame which is done by fully fledged TDLDA (see Sec. I C). Perturbation theory was only invoked for the purpose of deriving the averaging scheme.

The expression (8) shows the orientation-averaged cross section for emission from one particular single-electron state ϕ_i. The total cross section is obtained simply by adding up incoherently the contributions from each occupied state, thus yielding

$$\overline{\frac{d\sigma}{d\Omega}} = \sum_{i=1}^{N_{\rm el}} \overline{\frac{d\sigma_i}{d\Omega}} = C_0 Y_{00}(\vartheta\varphi) + C_2 Y_{20}(\vartheta\varphi), \tag{11}$$

$$C_l = \sum_{i=1}^{N_{\rm el}} C^{(i)}_l. \tag{12}$$

We remind that $Y_{20} \propto P_2(\cos\vartheta)$, where P_2 is the Legendre polynomial of second order. The orientation-averaged cross sections (8) and (11) thus have the widely used general form of an isotropic term plus another term $\propto P_2$ delivering anisotropic emission, i.e.,

$$\overline{\frac{d\sigma}{d\Omega}} \propto 1 + \beta P_2(\cos\vartheta), \tag{13}$$

where β is called the anisotropy parameter. We can easily compute it in terms of our aforementioned expansion as

$$\beta = \sqrt{5}\,\frac{C_2}{C_0}, \quad \beta^{(i)} = \sqrt{5}\,\frac{C^{(i)}_2}{C^{(i)}_0}. \tag{14}$$

The anisotropy parameter is what remains after all: just one parameter characterizing the pattern of the orientation-averaged cross section.

It is interesting to explore the value β for limiting cases in order to better understand its meaning. The first extreme corresponds to a state ϕ_i with angular momentum $l = 0$ which is rotationally invariant. The distribution becomes pure $\cos^2\theta$ which conforms to a value of $\beta = 2$. This is obviously the largest possible value of β corresponding to a maximally "unperturbed" (because of isotropy of the wave function in cluster frame) electronic emission, and accordingly the one-photon process which is maximally aligned along the laser polarization. The other extreme corresponds to the case for which emission is maximally "antialigned," namely, maximally transverse with respect to the laser polarization axis. The angular distribution then becomes ideally pure $\sin^2\theta$ which conforms to a value of $\beta = -1$. Actual values of β lie in between these two extreme cases. An interesting case of course is provided by $\beta = 0$ which describes a purely isotropic orientation-averaged PAD.

B. Direct averaging as an alternative

A conceptually simpler, although computationally more expensive, method is a direct numerical orientation averaging according to Eq. (4). Rotation about the laser polarization axis (that is by the Euler angle α) does not require any additional TDLDA runs. This thus leaves averaging over the surface of a unit sphere represented by the Euler angles β and γ. The β-γ integration is approximated by a finite summation. To that end, the surface of the sphere is divided in segments around selected sampling directions. We consider several levels of precision. The lowest tow are a very coarse grid with the 6 orientations (0,0, ±1), (0, ±1,0), (±1,0,0) and a finer grid with the 18 orientations (0,0, ±1), (0,1, ±1), (1,0, ±1), (0, −1, ±1), (−1,0, ±1), (0, ±1,0), (±1,0,0), (±1,1,0), (±1, − 1,0). These orientations are displayed in Fig. 1. The corresponding area of the segment on the surface is used as a weight for the averaging. Clusters with highly symmetric configurations allow one to reduce the number of actual TDLDA calculations by using symmetry operations.

C. Numerical realization

The numerical solution of the (time-dependent) Kohn-Sham equations for the cluster electrons proceeds with standard techniques as described in [30,36]. The electronic wave functions and the spatial fields are represented on a Cartesian grid in three-dimensional coordinate space with grid spacing $0.8\,a_0$ for Na. The numerical box employed here has a size of $(96 \times 0.8\,a_0)^3$. The spatial derivatives are evaluated via fast Fourier transformation. The ground-state configurations were found by accelerated gradient iterations for the electronic

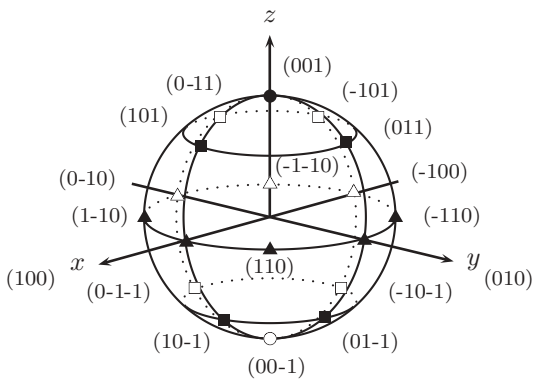

FIG. 1. Various orientations of the cluster used in the direct averaging scheme.

wave functions [37] and simulated annealing for the ions in the cluster. Dynamical propagation is done by the time-splitting method for the electronic wave functions [38], while the cluster ions are frozen during the analysis of angular distributions, which is fairly legitimate for the short time span of 120 fs used in our analysis. The mean field of TDLDA is augmented by a SIC. In practice, we use here average-density SIC, which was found to provide an efficient and reliable level of SIC [39].

The laser excitation is described by an external laser field

$$U_{\rm las} = -e\,\mathbf{r}\cdot\mathbf{e}_{\rm pol}\,E_0\sin^2\left(\frac{t}{T_{\rm pulse}}\pi\right)\sin(\omega_{\rm las}t), \qquad (15)$$

which is only activated in the time interval $0 \leqslant t \leqslant T_{\rm pulse}$. The field strength E_0 is related to the intensity I as $I/(\mathrm{W\,cm^{-2}}) = 27.8[E_0/(\mathrm{V\,cm^{-1}})]^2$. We use moderate intensities to keep one-photon processes in the perturbative regime in accordance with the presumptions of Sec. I A. The total pulse length $T_{\rm pulse}$ corresponds to a full width at half (intensity) maximum as $\mathrm{FWHM} \approx T_{\rm pulse}/3$. We use here $T_{\rm pulse} = 60$ fs and continue the time propagation until $t = 120$ fs before we collect the information on emitted electrons.

Electrons emitted from the cluster will eventually reach the boundaries of the box. In order to suppress re-feed of these electrons back into the box, we employ absorbing boundary conditions [29,30]. This is achieved by the mask function $\mathcal{M}(\vec{r})$:

$$\mathcal{M}(\vec{r}) = \left[\sin\left(\frac{R_{\rm box}-|\vec{r}|}{R_{\rm box}-R_{\rm cut}}\frac{\pi}{2}\right)\right]^{1/8} \times \Theta\,(R_{\rm box}-|\mathbf{r}|)\Theta(|\mathbf{r}|-R_{\rm cut}), \qquad (16)$$

where $\Theta(x)$ is the Heaviside function, $R_{\rm cut}$ is the cutoff radius outside which absorption starts, and $R_{\rm box}$ is the minimal radial distance from the origin to the closest point on the boundaries. The Kohn-Sham time step actually performed with the time-splitting method [38] is thus augmented by an absorbing step as

$$\tilde{\phi}_i = \hat{U}^{TV}\phi_i(t) \rightarrow \phi_i(t+\delta t) = \mathcal{M}(\vec{r})\tilde{\phi}_i, \qquad (17)$$

where $\hat{U}^{TV}$ is the unitary propagation operator. Applying the mask function $\mathcal{M}$ to the orbitals gently removes density approaching the box boundary and prevents it from being reflected. The absorption typically takes place over several grid points in order to avoid possible spurious reflection of outgoing wave functions and to provide sufficiently smooth overall behaviors [40]. Actually we use eight grid points corresponding to an absorbing zone of 6.4 a_0.

To compute the angular distribution of emitted electrons, the absorbed density is accumulated for each state and each (absorbing) grid point as

$$\Gamma_i(\vec{r}) = \int_0^\infty dt\;\gamma_i(\vec{r},t)\;, \qquad (18)$$

$$\gamma_i(\vec{r},t) = |[1-\mathcal{M}(\vec{r})]\hat{U}^{TV}\phi_i(t)|^2. \qquad (19)$$

By definition of $\mathcal{M}$, the field $\Gamma_i(\vec{r})$ is nonvanishing only in the spherical absorbing zone. The angular distribution of emitted electrons is finally gathered by dividing the absorbing zone into radial segments S_ν and integrating $\Gamma_i(\vec{r})$ over those segments. The photoelectron cross section thus becomes

$$\frac{d\sigma_i}{d\Omega} \sim \frac{1}{||S_\nu(\vartheta\varphi)||}\int_{S_\nu} d\mathbf{r}'\,\Gamma_i(\mathbf{r}')\;, \qquad (20)$$

where $||S_\nu(\vartheta\varphi)||$ denotes the area of the segment S_ν on the surface of a unit sphere. We finally define the total net ionization, or the number of escaped electrons, as the integral of Eq. (20) over Ω and summed over all states i:

$$N_{\rm esc} = \sum_i \sigma_i. \qquad (21)$$

II. RESULTS AND DISCUSSION

A. Na_3^+ as a simple test case

As a first and simplest test case, we consider Na_3^+ in the spherical jellium model. The two electrons occupy the $1s$ state with the wave functions

$$\phi_i = R_{10}(r)Y_{00}\chi_{\sigma_i},$$

where χ_{σ_i} are Pauli spinors. This state is rotationally invariant. Rotational averaging is thus not necessary here. The one-photon excitation augments this with Y_{10}. The outgoing wave is then

$$\psi_{\rm out} \propto Y_{10} \propto \cos\vartheta \Rightarrow \frac{\overline{d\sigma}}{d\Omega} \propto \cos^2\vartheta \Rightarrow \beta = 2.$$

This is a case of maximum possible anisotropy.

The spherical Na_3^+ is a strongly hypothetical system. A realistic Na_3^+ cluster with ionic background shows a pronounced planar structure as indicated in Fig. 2.This has dramatic effects on the angular distributions. Figure 2 shows distributions (see middle column) for three different orientations (displayed in the left column). There are pronounced and nontrivial structures in both angles ϑ and φ. Orientation averaging is clearly necessary in this case.

The upper right panel of Fig. 2 shows the result of a direct average over six orientations according to the scheme as outlined in Sec. I B, namely, the three orientations shown in the left column plus their three reflection pendants. We expect from Eq. (13) that an averaging over many orientations should yield a φ-independent distribution. We observe here that the average over only six orientations already wipes out the φ dependence to a large extend.

We now go for the explicit averaging over 18 orientations (see Sec. I B and Fig. 1). The result is plotted in the middle right panel of Fig. 2. We obviously noticed that the faint φ dependence has been wiped out even better than in the case of only 6 orientations. The lower right panel finally shows the fully orientation-averaged result produced according to the "exact" averaging procedure of Sec. I A. It smoothes the distributions dramatically, yielding at the end an anisotropy of $\beta = 1.83$. Note that the direct 18-orientation averaging here already gives a pattern which is very close to the "exact" scheme.

We have just seen from Fig. 2 that any averaging wipes out efficiently any structure in the angle φ. Figure 3 compares the ϑ dependence for various approaches. Benchmark is the result obtained from applying the "exact" averaging procedure

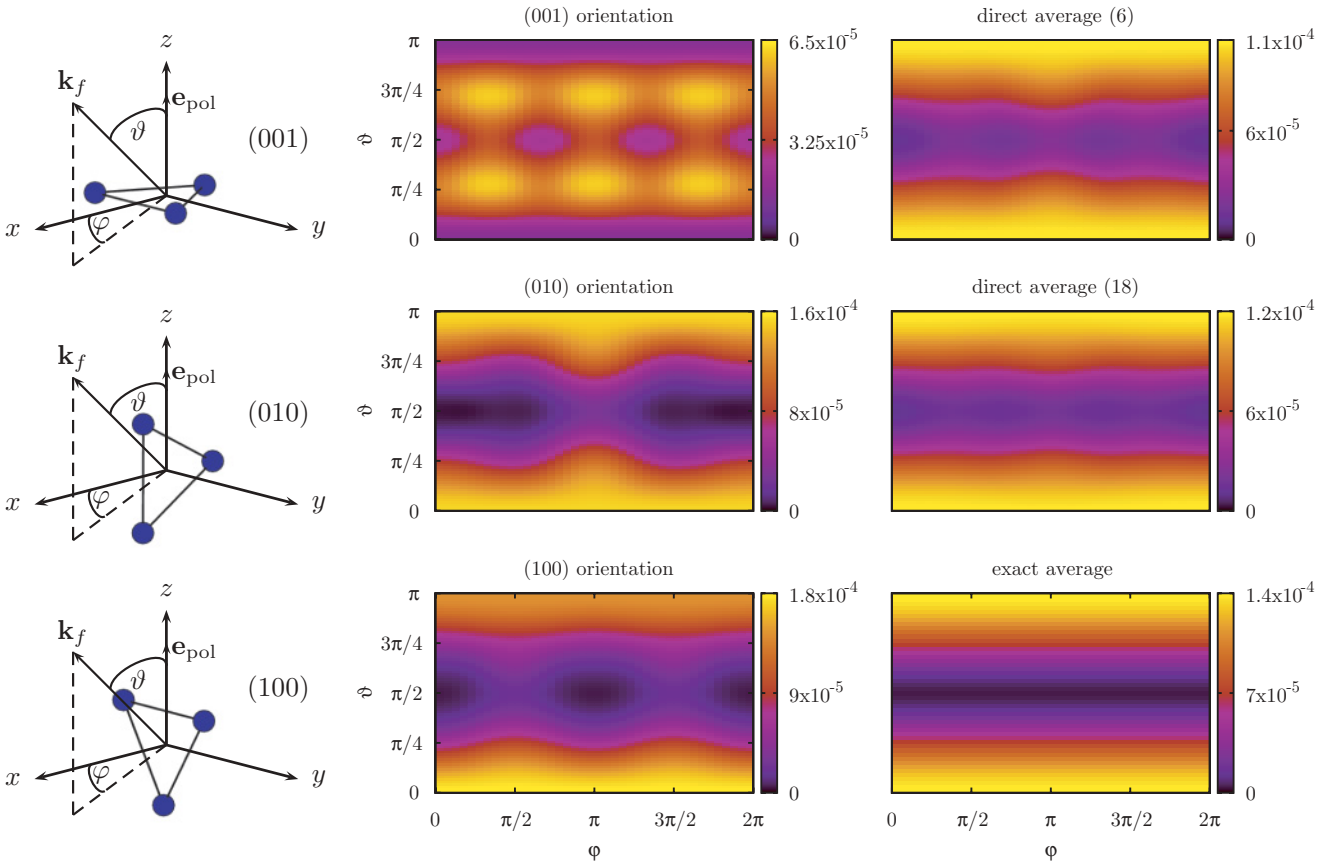

FIG. 2. (Color online) Photoelectron angular distributions of Na_3^+ irradiated by a laser of FWHM = 20 fs, intensity $I = 3.2 \times 10^{11}$ W/cm^2, and frequency $\omega_{\rm las} = 11.6$ eV. Left column: Orientations (001), (010), (100) with respect to the laboratory frame. Middle column: PAD for each orientation. Right column: Top, direct average over 6 orientations (the three shown plus their reflection pendants); middle, direct average over 18 orientations; bottom, exact scheme.

of Sec. I A which requires as an input the cross sections from six independent laser polarizations. The alternative direct averaging over orientations is also plotted in Fig. 3. It shows nicely the typical pattern of Eq. (13) and the anisotropy comes already fairly close to the exact result. The sparser direct averaging over six reference orientations shows deviations from the exact result, although they remain small, as was already observed in Fig. 2.

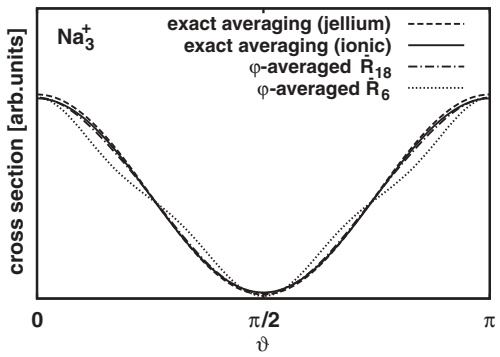

FIG. 3. Angular distributions along ϑ for Na_3^+ (same laser parameters as in Fig. 2) for various averaging schemes: exact averaging (with ionic or jellium background) and the direct averaging over 6 or 18 orientations (with ionic background).

B. Systematics in small Na clusters

The case of Na_3^+ has provided interesting insight into our approach. It is now time to apply it to a larger variety of systems and to explore how orientation-averaged PAD brings information on cluster properties. We have chosen to discuss small Na clusters as examples. Among the interesting properties to explore, cluster deformation is a natural quantity to investigate. It is in particular interesting to see how deformation may be related to the anisotropy parameter β. We also briefly sketch the electronic properties (single-electron energies) of the clusters under consideration.

The most important ground-state properties for the following studies are the global cluster deformation and the spectra of the occupied single-electron states (from which the electrons are lifted into the continuum through the laser field). The deformation itself is characterized by the total quadrupole momentum of the ionic (or jellium) background. The geometry is best quantified by the dimensionless moment α:

$$\alpha = \sqrt{\sum_{m=-2}^{2} \alpha_{2m}}, \quad \alpha_{2m} = 4\pi \overline{r^2 Y_{2m}}/5Nr_{\rm rms}^2, \tag{22}$$

where $r_{\rm rms}$ is the rms radius of the background and N the number of ions. This will be discussed later on in connection with Fig. 5.

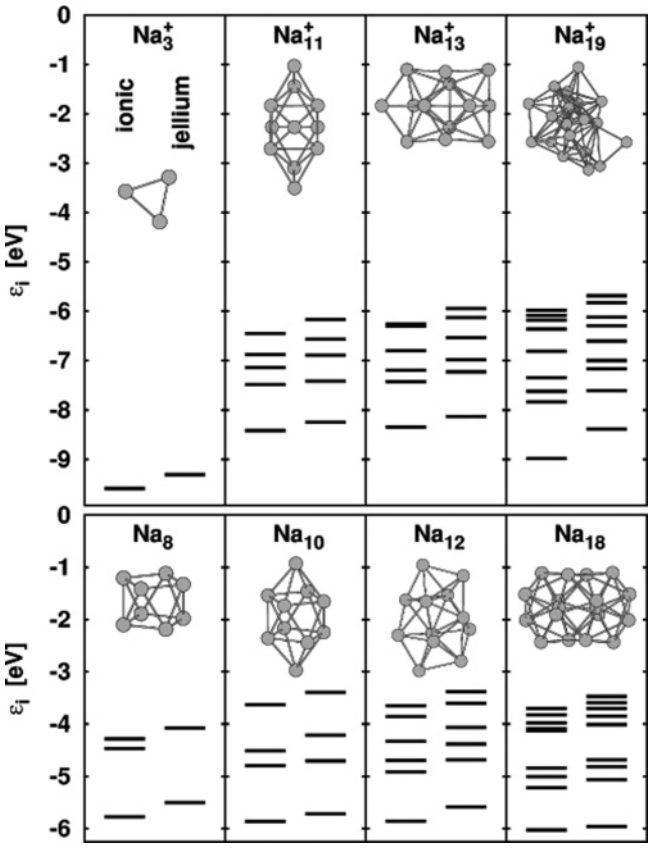

FIG. 4. Ground-state spectra of the occupied single-electron states for the systems considered in this paper. Left columns in each panel: Spectra for the electron cloud with detailed ionic background. Right columns in each panels: Spectra from the equivalent jellium model.

In the following, we show results for a few selected Na clusters using, as it should be, detailed ionic structure which was optimized by simulated annealing. For comparison, we also show for the same clusters results from a deformed jellium model with soft surface [30,41]. The jellium deformation is adjusted such that the quadrupole moments (of the electronic density) become the same as the ones computed with full ionic background. A surface thickness of 1 a_0 was chosen such that the single-electron energies and the optical response are comparable to the fully ionic description.

1. Single-electron spectra

The ground-state single-electron energies ε_i for all considered cases are shown in Fig. 4.The cluster cations (upper panels) have, of course, an ionization potential (IP) much larger than that of the neutral species. The spectral span between the deepest bound state and the highest occupied molecular orbital (HOMO) is about the same in all systems (except, of course, for Na_3^+ which has only one occupied state). The spectral density increases with system size and is very similar for ionic background (left columns) versus jellium (right columns).

2. Trends in relation to deformation

In order to stay safely in the regime of one-photon emission for all occupied states, we use the laser frequency $\omega_{\rm las} = 7.5$ eV

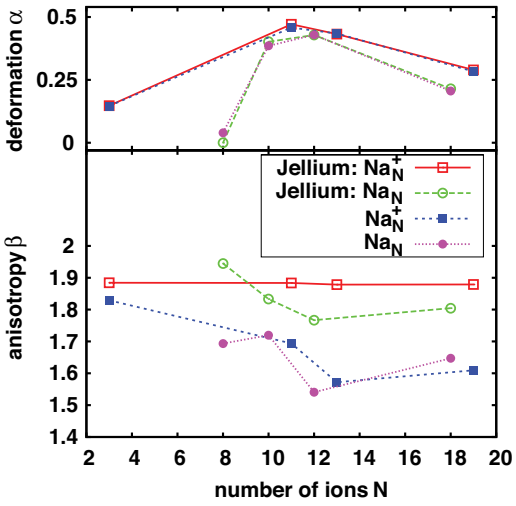

FIG. 5. (Color online) Anisotropy parameter β (bottom) defined in Eq. (13) and quadrupole deformation α (top) defined in Eq. (22) as a function of Na cluster size N, for neutral (squares) and positively charged (circles) species. Open symbols correspond to a jellium background, while the solid ones result from a full ionic background.

for neutral clusters and $\omega_{\rm las} = 10$ eV for cationic clusters and the laser intensity $I = 10^{11}$ W/cm^2 (unless explicitly said otherwise, e.g., Na_3^+ in the previous section). This corresponds to a net ionization $N_{\rm esc}$ of 0.0001–0.009.

As shown analytically in Sec. I A and confirmed practically in Sec. II A, the orientation-averaged cross section from one-photon processes can be characterized in terms of one single anisotropy parameter β. Figure 5 summarizes the anisotropy parameter β for neutral clusters Na_N and cationic clusters Na_N^+ (bottom panel) and shows it together with the corresponding quadrupole deformation α (top panel) defined in Eq. (22). The latter parameter stands here as an indicator of the electronic cloud structure.

The selection of clusters in Fig. 5 covers a wide range of deformation and electronic configurations. Except for Na_3^+, the global deformation α is basically determined by the electronic structure [41,42]. Na_8 has a magic electron number $N_{\rm el} = 8$. The closed spherical electron shells drive the background to nearly spherical shape and thus the quadrupole deformation α is zero. The other magic system in the sample is Na_3^+ with $N_{\rm el} = 2$. But here the planar ionic configuration overrules the electronic trend to sphericity as we have already mentioned in Sec. II A. The clusters with $N_{\rm el} = 10$ are strongly prolate and close to axial symmetry, while those with $N_{\rm el} = 18$ are weakly prolate, and the samples with $N_{\rm el} = 12$ are triaxial. It ought to be mentioned that these triaxial systems have a very small HOMO-LUMO (lowest unoccupied molecular orbital) gap, indicating that their electronic structure is somewhat volatile with a great variety of isomers nearby [43].

Figure 5 shows little variation of β within the clusters described with detailed ionic structure. Even less variation is observed within the group of jellium results. The charge state also seems to play no role. The major difference is seen between the jellium model and the detailed ionic background. The jellium results all gather around $\beta \sim 1.9$ close to the maximum possible anisotropy while ionic structure causes

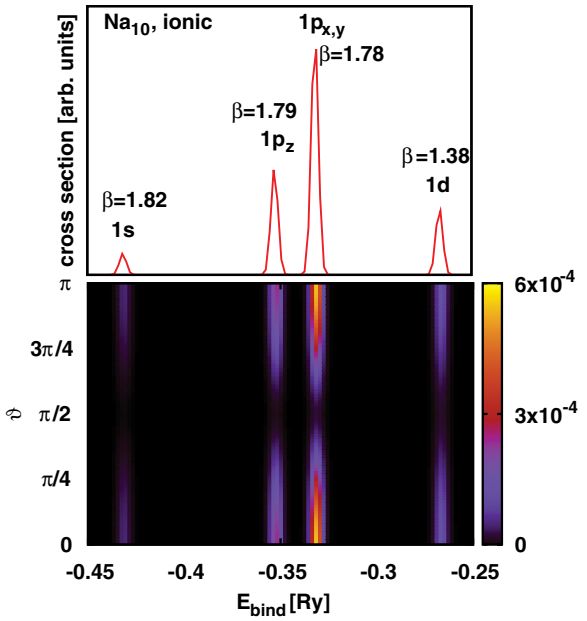

FIG. 6. (Color online) Energy-resolved angular distribution of Na_{10}. Upper panel: Photoelectron spectrum. Lower panel: Combination of photoelectron spectrum and angular distribution; the horizontal axis shows the energy and the vertical axis shows the angle ϑ.

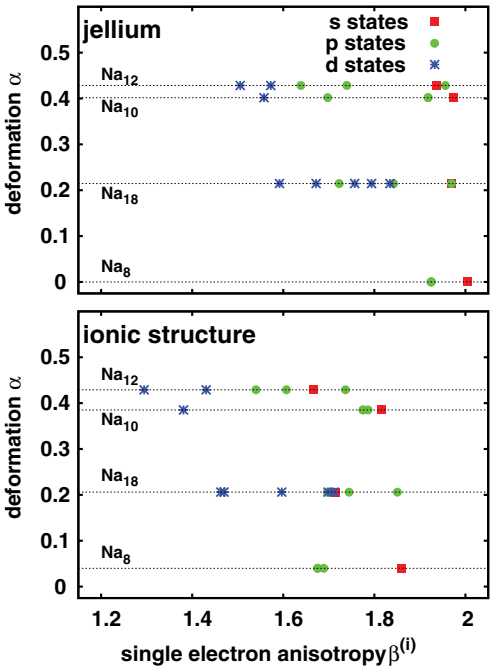

FIG. 7. (Color online) State-dependent anisotropies $\beta^{(i)}$ for the neutral clusters Na_8, Na_{10}, Na_{12}, and Na_{18}. For better discrimination, the anisotropies are grouped according to the global quadrupole deformation α. The single-electron states are associated with s, p, and d states of a spherical mean field. Lower panel: Result from calculation with full ionic background. Upper panel: Jellium results.

significantly lower values around $\beta \sim 1.6$. The discrepancies between both models also seem to increase slowly with cluster size, especially for cationic clusters. This means that explicit ions in the background produce more isotropic (but still prolate) PAD. The ionic perturbations seem to rescatter the electronic waves and thus cumulate a strong isotropic component. However the cases with $N_{el} = 12$ fall a bit below the generally smooth trend. This is probably due to the particularly soft electronic structure of these triaxial clusters which makes the electrons extremely responsive to any small perturbation.

The basic conclusion at that level is that the global anisotropy β does not show any clear dependence on the total deformation α. This indicates that the global anisotropy β is too much an averaged quantity, thus possibly not highly discriminating. The next (more detailed) step is to consider $\beta^{(i)}$ state by state, or, experimentally speaking, energy resolved.

3. *Energy-resolved orientation-averaged PAD*

An example of energy-resolved orientation averaged PAD is shown in Fig. 6 in the case of Na_{10}. Calculations have been performed with full ionic background. The figure provides a rather complete picture of electronic emission pattern. Single-electronic states are very clearly identified, each associated with a well-defined β value. One observes that the anisotropies $\beta^{(i)}$ decrease with increasing complexity of state (i.e., from $1s$ over $1p$ to $1d$). It is interesting to consider these trends in the state-dependent $\beta^{(i)}$ values in a more systematic way. A quick glance at Fig. 4 shows that, in all cases, the levels are grouping into three different energy shells (with more or less energy span depending on deformation) and we thus associate "spherical" quantum numbers to the level groups: s for the deepest bound state, p for next group, and d for the highest levels (if occupied).

Figure 7 shows the anisotropies $\beta^{(i)}$ for all occupied electronic states in detail, and for various clusters. It is obvious that the span of anisotropies grows from s over p to the d shell and the larger span extends to lower $\beta^{(i)}$. This is probably caused by the increasingly complex structure of these higher electronic states. The trend is the same with full ionic background and with the jellium model, although the results with ionic background are shifted as a whole to lower $\beta^{(i)}$ in accordance with the lower total β. The decrease of average anisotropy with increasing level number corresponds nicely to the weak trend with system size seen in Fig. 5. It is, furthermore, interesting to note that the span between the state with the highest $\beta^{(i)}$ and the lowest one increases somewhat with deformation. It seems that the interplay between complexity of a state and deformation cooperates to enhance the effect on lowering anisotropy.

C. Direct orientation averaging

We have focused the preceding discussions on simple metal (Na) clusters in a specific dynamical regime, namely, the perturbative one-photon regime. Laser irradiation of clusters can, however, cover a much wider range of systems and dynamical regimes. We want to make here a preliminary exploration of these aspects. The most important point is the extension of our approach to nonperturbative and multiphoton regimes and we shall thus focus on this aspect in the following.

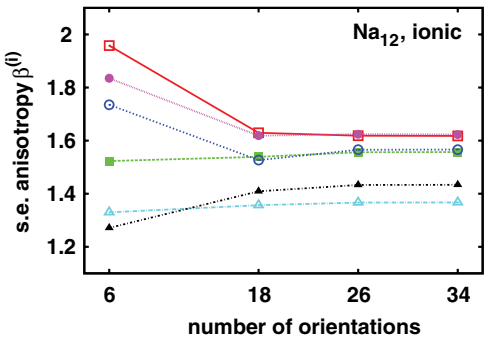

FIG. 8. (Color online) Single-electron anisotropies for Na_{12} excited by a strong laser pulse with $\omega_{las} = 7.5$ eV, $T_{pulse} = 60$ fs, and intensity $I = 10^{13}$ W/cm^2, which is already in the nonlinear regime yielding an averaged net ionization of $N_{esc} = 0.7$ electrons. Results are drawn as a function of the number of averaged orientations.

1. Convergence of direct orientation-averaged PAD

The "exact" procedure detailed in Sec. I A has been derived in the perturbative regime and cannot be applied to nonperturbative cases. We have nevertheless seen that a direct averaging procedure provides very similar results for an acceptably limited number of well-chosen orientations. This direct procedure (see Sec. I B) remains in turn fully applicable to the nonperturbative regime. The remaining question is how many orientations are necessary to reach a final answer? In this case, no benchmark is available and the single way to validate the method is to explore the convergence of results with the number of orientations..

An example is shown in Fig. 8 in the case of Na_{12}. As discussed previously, the key quantity for full PAD-PES is the state-dependent $\beta^{(i)}$ rather than the global β. We have thus chosen to consider this quantity as a function of the number of computed orientations. The convergence of the results is obvious. Up to details, we find again that 18 orientations represents a nearly optimum number, yielding a good compromise between expense and averaging. Using around 30 orientations yields a fully converged result. We have also checked that this converged value indeed differs from that obtained by the exact (thus non-exact here, values not shown) procedure, as expected.

Having now at hand a reliable scheme for exploring nonperturbative regimes, we want to present two examples of application. We first study in the next section the impact of laser intensity, at fixed photon frequency. And as a second step (see Sec. II C 2), we consider effects of photon frequency variation.

2. Na_8 toward the multiphoton regime

The comparison in Fig. 3 has shown that the direct averaging, although more expensive, can produce reliable results if the mesh of orientations is chosen to be dense enough. This allows one to consider multiphoton processes without developing the corresponding averaging schemes from multiphoton perturbation theory. Figure 9 compares the orientation-averaged cross sections (direct averaging with 18 reference orientations) from Na_8 as a function of intensity and for two frequencies near the one-photon threshold for

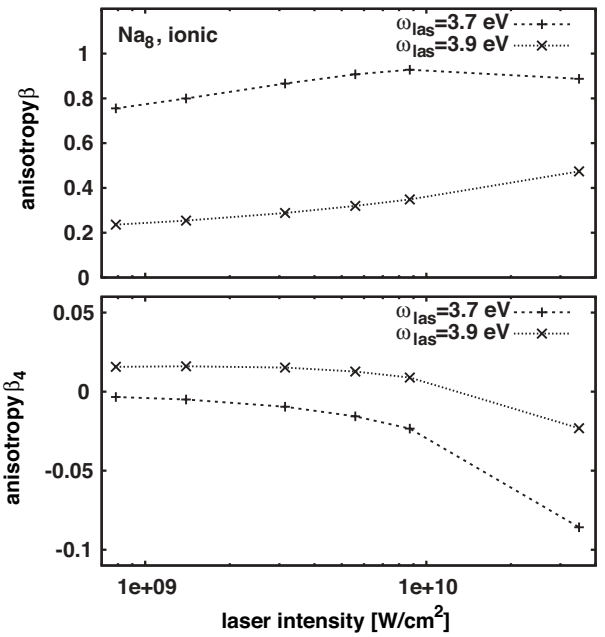

FIG. 9. Results from direct orientation-averaged PAD in Na_8 drawn as a function of laser intensity. Two laser frequencies are considered as indicated. The pulse length was 60 fs. Lower panel: Hexadecapole anisotropy β_4. Upper panel: Quadrupole anisotropy $\beta \equiv \beta_2$.

which we have a good chance that the two-photon processes become increasingly important with increasing intensity. The net ionization was about $N_{esc} = 0.001$–0.1. The orientation-averaged PAD can be expanded in general as

$$\overline{\frac{d\sigma}{d\Omega}} \propto 1 + \sum_{l=2,4,\ldots} \beta_l P_l(\cos\vartheta), \tag{23}$$

where the lowest order is the (quadrupole) anisotropy $\beta_2 \equiv \beta$. Higher orders come into play with increasing photon number. The anisotropy shows a gentle trend with intensity, mostly increasing except for the last point in the case of $\omega_{las} = 3.7$ eV. More interesting is the appearance of nonzero β_4 for the higher intensities, which is a clear signal for the onset of two-photon processes. We also see that the two slightly different frequencies deliver significantly different values. There thus is a strong frequency dependence. Both dependencies, on intensity and on frequency, thus promise to show rich pattern [15]. This will be studied in detail in forthcoming publications. The present example has demonstrated that the methods developed here provide appropriate tools for that.

III. CONCLUSION AND OUTLOOK

We have investigated PADs for Na clusters, neutral and positively charged. The basis of the description is the TDLDA for the valence electrons of the cluster augmented by SIC. The short laser pulses used here allow one to keep the ionic configuration as frozen during each TDLDA-SIC calculation. We consider free Na clusters for which the orientation is not known *a priori*. We deal thus with an isotropic ensemble of free clusters. An analytical scheme for computing the orientation-averaged PAD is developed for one-photon processes. It

reduces the computational expense to only six TDLDA-SIC calculations for appropriately chosen reference orientations. Additionally, we have also studied direct averaging by representing the averaging integral on a finite mesh of orientations, considering several levels of refinement.

The formal result in the perturbative regime is that orientation-averaged PADs from one-photon processes are fully characterized by one parameter for anisotropy β (the quadrupole component in the PAD). Anisotropy was analyzed as a global quantity or state resolved. We investigated the systematics of the global anisotropy parameter with varying cluster size for Na clusters in the range $N = 3, \ldots, 19$. There is only a weak dependence on cluster size and charge state. However, comparison with results from a soft jellium background (with exactly comparable deformation in each case) shows a dramatic effect from the detailed ionic background. While the jellium model produces always large anisotropies, near the maximum possible, the detailed ionic background reduces these anisotropies by about 25%. It seems that the ionic perturbation induces rescattering processes which produce an isotropic background. We have also analyzed the anisotropies on a state-by-state basis and found that the anisotropy is largest for the most deeply lying states and decreases gently, but systematically, with moving up toward the energy of the occupied orbital. The reason for this trend is most probably the increasing complexity of the state with increasing energy. The effect turns out to be somewhat more pronounced in strongly deformed clusters.

The exact scheme is used to benchmark a direct orientation averaging on a finite mesh in orientation space (surface of a sphere). It turns out that a very good reproduction of the PAD can be already achieved with about 30 reference orientations. A smaller mesh with 18 orientations represents a good compromise between expense and precision. The number of TDLDA-SIC calculations can be reduced by exploiting structural symetries if there are any (as, e.g., in the highly symmetrical Na_8 cluster). This result shows the enormous savings obtained with the partially analytical treatment for one-photon processes. And it also proves the validity of direct averaging on still acceptably sparse grids in orientation space, where about 30 reference orientations yield converged results and already 18 orientations suffice for an acceptable description in practice. We have thus applied in a test for Na_8 direct averaging to PAD in the transition from a perturbative to a nonlinear regime. We find a growth of the hexadecapole component in the PAD with increasing laser intensity.

The present paper constitutes an exploration of orientation-averaged PADs. There are several interesting questions left open to be investigated in subsequent works. The two major directions are, first, to work out the frequency dependence of the anisotropy in a systematic manner and, second, to vary the materials in order to explore the influence of the ionic background.

ACKNOWLEDGMENTS

This work was supported by the Deutsche Forschungsgemeinschaft (RE 322/10-1, RO 293/27-2), by the Humboldt Foundation, and by the French Agence Nationale pour la Recherche (ANR-06-BLAN-0319-02). Some of the calculations have been performed at the French computational facility CalMiP (Calcul en Midi-Pyrénées).

[1] M. Brack, Rev. Mod. Phys. **65**, 677 (1993).
[2] W. A. de Heer, Rev. Mod. Phys. **65**, 611 (1993).
[3] U. Kreibig and M. Vollmer, *Optical Properties of Metal Clusters*, Springer Series in Materials Science, Vol. 25 (Springer, Berlin, 1993).
[4] H. Haberland, Ed., *Clusters of Atoms and Molecules 1—Theory, Experiment, and Clusters of Atoms*, Springer Series in Chemical Physics, Vol. 52, (Springer, Berlin, 1994).
[5] K. M. McHugh, J. G. Eaton, G. H. Lee, H. W. Sarkas, L. H. Kidder, J. T. Snodgrass, M. R. Manaa, and K. H. Bowen, J. Chem. Phys. **91**, 3792 (1989).
[6] D. L. Lichtenberger, K. W. Nebesny, C. D. Ray, D. R. Huffman, and L. D. Lamb, Chem. Phys. Lett. **176**, 203 (1991).
[7] J. Pinaré, B. Baguenard, C. Bordas, and M. Broyer, Eur. Phys. J. D **9**, 21 (1999).
[8] B. Baguenard, J. C. Pinaré, C. Bordas, and M. Broyer, Phys. Rev. A **63**, 023204 (2001).
[9] J. R. R. Verlet, A. E. Bragg, A. Kammrath, O. Cheshnovsky, and D. M. Neumark, J. Chem. Phys. **121**, 10015 (2004).
[10] J. Wills, F. Pagliarulo, B. Baguenard, F. Lépine, and C. Bordas, Chem. Phys. Lett. **390**, 145 (2004).
[11] C. Bordas, B. Baguenard, B. Climen, F. Lépine, F. Pagliarulo, M. M. Lebeault, and J. Wills, Intern. J. Mod. Phys. B **19**, 2899 (2005).
[12] F. Pagliarulo, B. Climen, B. Baguenard, F. Lépine, M. Lebeault, A. Ollagnier, J. Wills, and C. Bordas, Int. J. Mass Spectrosc. **252**, 100 (2006).
[13] M. Kjellberg, O. Johansson, F. Jonsson, A. V. Bulgakov, C. Bordas, E. E. B. Campbell, and K. Hansen, Phys. Rev. A **81**, 023202 (2010).
[14] O. Kostko, C. Bartels, J. Schwobel, C. Hock, and B. von Issendorff, J. Phys.: Conf. Ser. **88**, 012034 (2007).
[15] C. Bartels, C. Hok, J. Huwer, R. Kuhnen, J. Schwöbel, and B. von Issendorff, Science **323**, 1323 (2009).
[16] H. Bethe, *Handbuch der Physik, Band 24/1* (Springer, Berlin, 1933).
[17] F. H. M. Faisal, *Theory of Multiphoton Processes* (Plenum, New York, 1987).
[18] J. Cooper and R. N. Zare, J. Chem. Phys. **48**, 942 (1968).
[19] J. Cooper and R. N. Zare, J. Chem. Phys. **49**, 4252 (1968).
[20] P. Ghosh, *Introduction to Photoelectron Spectroscopy* (Wiley, New York, 1983).
[21] A. V. Solov'yov, R. G. Polozkov, and V. K. Ivanov, Phys. Rev. A **81**, 021202(R) (2010).
[22] T. Seideman, J. Chem. Phys. **107**, 7859 (1997).
[23] T. Seideman, Annu. Rev. Phys. Chem. **53**, 41 (2002).
[24] Y. Suzuki and T. Seideman, J. Chem. Phys. **122**, 234302 (2005).

[25] F. Calvayrac, P.-G. Reinhard, and E. Suraud, Phys. Rev. B **52**, R17056 (1995).
[26] K. Yabana and G. F. Bertsch, Phys. Rev. B **54**, 4484 (1996).
[27] F. Calvayrac, P.-G. Reinhard, and E. Suraud, Ann. Phys. (NY) **255**, 125 (1997).
[28] J. P. Perdew and A. Zunger, Phys. Rev. B **23**, 5048 (1981).
[29] C. A. Ullrich, J. Mol. Struct. (THEOCHEM) **501–502**, 315 (2000).
[30] F. Calvayrac, P.-G. Reinhard, E. Suraud, and C. A. Ullrich, Phys. Rep. **337**, 493 (2000).
[31] A. Pohl, Ph.D. thesis, Friedrich-Alexander Universität, Erlangen/Nürnberg, 2003.
[32] A. Pohl, P.-G. Reinhard, and E. Suraud, Phys. Rev. A **70**, 023202 (2004).
[33] E. Giglio, P.-G. Reinhard, and E. Suraud, Phys. Rev. A **67**, 043202 (2003).
[34] M. Bär, P. M. Dinh, L. V. Moskaleva, P.-G. Reinhard, N. Rösch, and E. Suraud, Phys. Rev. B **80**, 195404 (2009).
[35] A. R. Edmonds, *Angular Momentum in Quantum Mechanics* (Princeton University Press, Princeton, 1957).
[36] P.-G. Reinhard and E. Suraud, *Introduction to Cluster Dynamics* (Wiley, New York, 2003).
[37] V. Blum, G. Lauritsch, J. A. Maruhn, and P.-G. Reinhard, J. Comp. Phys. **100**, 364 (1992).
[38] M. D. Feit, J. A. Fleck, and A. Steiger, J. Comput. Phys. **47**, 412 (1982).
[39] C. Legrand, E. Suraud, and P.-G. Reinhard, J. Phys. B **35**, 1115 (2002).
[40] P.-G. Reinhard, P. D. Stevenson, D. Almehed, J. A. Maruhn, and M. R. Strayer, Phys. Rev. E **73**, 036709 (2006).
[41] B. Montag, P.-G. Reinhard, and J. Meyer, Z. Phys. D **32**, 125 (1994).
[42] H. Haberland and M. Schmidt, Eur. Phys. J **6**, 109 (1999).
[43] C. Kohl, B. Montag, and P.-G. Reinhard, Z. Phys. D **35**, 57 (1995).